

Article

Extraction of Iron and Alumina from Red Mud with a Non-Harmful Magnetization Sintering Process

Rui Chen ^{1,2}, Lin Shi ^{1,2,3,*}, Haoyong Huang ^{1,2} and Jie Yuan ^{1,2}¹ School of Environment and Energy, South China University of Technology, Guangzhou 510006, China² The Key Lab of Pollution Control and Ecosystem Restoration in Industry Clusters, Ministry of Education, South China University of Technology, Guangzhou 510006, China³ Zhongshan Institute of Modern Industrial Technology of SCUT, Zhongshan 528400, China

* Correspondence: celshi@scut.edu.cn

Abstract: Red mud, which could cause numerous problems to the environment, is a hazardous waste generated from the alumina smelting industry. In general, the storage and harmless utilization of red mud are hard to implement due to its fine particle size and high alkalinity. This study put forward a novel process to separate iron (MgFe_2O_4) and alumina (Al_2O_3) in red mud by a magnetization sintering method. The magnesium oxide was added to transform the nonmagnetic Fe_2O_3 into magnetic MgFe_2O_4 to achieve physical separation of iron-bearing minerals, and the alumina-bearing minerals were converted into dissoluble NaAlO_2 minerals in a one-step reaction. The atmospheric pressure leaching process was adopted in this study for alumina resource recovery. To achieve clean alumina production, the silicate in the leaching solution was removed by adding the slightly soluble CaSO_4 , and the entire process becomes clean and harmless. The feasibility of the process was verified by thermodynamic analysis, and a series of experiments were performed to detect the optimum $\text{MgO}/(\text{Fe}_2\text{O}_3 + \text{MgO})$ ratio and the calcining and leaching conditions. The morphological and mineralogical characteristics of modified red mud, leaching red mud, and magnetic separation product were studied by X-ray diffraction analysis (XRD) and scanning electron microscopy (SEM) energy dispersive spectroscopy (EDS). It was observed that under the optimal conditions with $\text{MgO}/(\text{Fe}_2\text{O}_3 + \text{MgO})$ of 14.89% to recover iron and aluminum, the corresponding recovery rates were 67.54% and 73.01% respectively, and the iron grade was 30.46%. The EDS results showed that the obtained Mg/Fe ratio of the magnetic separation product was 0.4677–0.528, which is slightly different from that of the standard MgFe_2O_4 at 0.5. This new method can promote the development of comprehensive utilization of red mud and iron production.

Keywords: red mud; harmless utilization; mineralogical analysis; MgFe_2O_4 ; leaching parameter

Citation: Chen, R.; Shi, L.; Huang, H.; Yuan, J. Extraction of Iron and Alumina from Red Mud with a Non-Harmful Magnetization Sintering Process. *Minerals* **2023**, *13*, 452. <https://doi.org/10.3390/min13030452>

Academic Editor: Brajendra Mishra

Received: 14 February 2023

Revised: 9 March 2023

Accepted: 16 March 2023

Published: 22 March 2023



Copyright: © 2023 by the authors. Licensee MDPI, Basel, Switzerland. This article is an open access article distributed under the terms and conditions of the Creative Commons Attribution (CC BY) license (<https://creativecommons.org/licenses/by/4.0/>).

1. Introduction

Red mud is the waste discharged from the alumina smelting industry during the Bayer process, and it has high alkalinity ($\text{pH} > 12$) and heavy metals such as Cr, Cd, Pb, As, and Hg [1]. Red mud dumps can occupy lots of the land, create dust, alkalize the land, and contaminate the groundwater. Approximately 1–2.5 tons of Bayer red mud are generated when producing 1 ton of alumina. Globally, about 175.5 Mt of red mud are discharged annually with an increasing trend in the next few years, which has restricted the development of the alumina industry [2,3]. In recent years, researchers have proposed various treatment methods to reduce the pollution from red mud. Due to the chemical curing and hydraulicity of amorphous silicates [4], red mud can be used as raw materials for ceramics, light aggregates, and geological polymers [5–7]. Moreover, as red mud also has a large specific surface area and adsorption capacity, it can be modified as environmental remediation materials (RM-ERMs) to achieve the purpose of “waste to waste” [8,9]. In addition, red mud can also be utilized in the field of catalysis [10,11].

The Bayer red mud also has a complex composition, mainly including sesquioxide (Al_2O_3 and Fe_2O_3), sodium oxide (Na_2O), titanium oxide (TiO_2), and silicon oxide (SiO_2) at a total content of more than 70%, along with various trace elements (Sc, Ga, V, and Zr). Recovery of valuable elements from red mud is promising under the situation of increasingly depleted natural resources [12]. However, recovering these elements from red mud is challenging due to the gradual and uniform distribution of the valuable components in the mineral phase of red mud during crushing and Bayer leaching cycles [13]. Hydrogrossular ($\text{Ca}_3\text{Al}_2(\text{SiO}_4)_{3-x}(\text{OH})_{4x}$), diaspore ($\alpha\text{-AlOOH}$), and boehmite ($\gamma\text{-AlOOH}$) are the sources of alumina in red mud, and they have low solubility at atmospheric pressure. The original Al-Si or Al-O crystal structure must be destroyed to enhance alumina solubility. Bruckard et al. [14] recovered 55% of Al and 90% of Na through the smelting process at 1400°C ; Li et al. [15] recovered 89.71% of alumina using the lime-soda sintering process at $1000\text{--}1050^\circ\text{C}$ for 90 min; Liu et al. [16] investigated the effect of Ca content on the dissolution of alumina and sodium during the sintering process and demonstrated that the activity of SiO_2 decreased as the Ca/Si ratio increased to 1.98. Pei et al. [17] explored a low calcium sintering process of red mud, and after sintering, leaching, and hydrothermal transition, the recovery rate of Al and Na reached 93% and 96%, respectively. These above-mentioned studies have already obtained some good achievements in the dissolution of Na and Al from red mud. Nevertheless, the sintering process enhances the dissolution of Al by adding calcium oxide to prevent the dissolution of Si [18], and the continuous dissolution of Si during the leaching process is still inadequately reported.

For iron-bearing red mud, researchers proposed a reduction roasting approach to transform hematite into magnetite, followed by magnetic separation to achieve enrichment of Fe minerals due to the magnetic susceptibility difference between iron/iron oxides and gangue minerals [19,20]. Rao et al. [21] investigated the effect of the reduction process by adding sodium carbonate and sodium sulfate and identified that the presence of sodium salts enhanced the growth of metallic iron grains to aggregate at larger sizes. Ding et al. [22] studied various parameters on the extraction of iron by segregation roasting-magnetic separation, where gaseous ferric chloride diffused through the surface of the coke and was reduced to metallic iron at high temperatures. The application of these methods has also raised some problems. Harmful gases emissions such as carbon monoxide (CO), chlorine (Cl_2), hydrogen sulfide (H_2S), and even arsenic hydride (AsH_3) seem to be ignored by previous researchers [23,24] when controlling the restorative atmosphere, and most previous studies are focused on the extraction rate only. The reduction reaction also requires an excessive amount of reductant to produce greenhouse gas (CO_2), thereby creating a challenge for the gas treatment in the entire process.

Magnesioferrite (MgFe_2O_4) is a strongly magnetic mineral that belongs to the magnetite system, and it can be synthesized by a solid-phase reaction of Fe_2O_3 and MgO at elevated temperatures. The crystal structure of magnesioferrite is with the formula $(\text{Mg}_{0.65}\text{Fe}_{0.35})_A[\text{Fe}_{1.65}\text{Mg}_{0.35}]_B\text{O}_4$ and the Mg^{2+} and Fe^{3+} cations are randomly distributed over its tetrahedral and octahedral sites [25]. Owing to its unique magnetic and high melting point properties, magnesioferrite has been used in many fields, such as biomedical, environmental protection, and refractory materials [26–28]. The iron minerals from red mud can be quickly transformed into MgFe_2O_4 by a one-step reaction to increase magnetism. Xue et al. [29] added 6% of SiO_2 to recover iron from basic oxygen furnace (BOF) slag, and the BOF phases were transformed into MgFe_2O_4 spinel and $\beta\text{-Ca}_2\text{SiO}_4$. The total Fe content was enhanced by 15.8%, from 21.20% to 37.00%. He et al. [30] investigated the different oxidation conditions under high temperatures for the recovery of MgFe_2O_4 from the BOF slag, the results indicated that the maximum recovery rate was achieved with an oxidation time of 100 min under an airflow rate of $1.25\text{ L}/\text{min}^{-1}$. Therefore, it is possible to separate MgFe_2O_4 from calcined slag. The method is a clean process compared to traditional reduction roasting without adding reductant to control the complex reduction atmosphere and the generation of harmful gases. The current research is aimed to recycle most of the alumina and iron remaining in the iron-bearing red mud. Therefore, combining

the Fe magnetization process with the lime-soda sinter process could have more practical significance for comprehensively utilizing the red mud. As the additives are cheap, widely sourced, and harmless, the entire process does not produce harmful gases. In this study, a series of experiments were performed to optimize the conditions for forming MgFe_2O_4 and the alumina extraction rate. The feasibility of the magnetization sintering process and the mineral phase transformation mechanism were explored. The developed magnetization sintering process has a few achievements as follows:

(1) A new method is proposed to separate the Fe-mineral (MgFe_2O_4) from red mud; (2) Lower sintering temperature and $\text{MgO}/\text{Fe}_2\text{O}_3$ mass fraction conditions are investigated in this research; (3) The optimal leaching condition, including the optimal leaching temperature, time, and liquid/solid(L/S) ratio, can provide some references for alkaline leaching; (4) The slightly soluble CaSO_4 was innovatively used instead of CaO or $\text{Ca}(\text{OH})_2$ to reduce silicate content; and (5) This process can solve the disposal problems for low-grade Fe-bearing red mud in the refineries and greatly reduce the emission of red mud.

2. Materials and Methods

2.1. Materials

The red mud (RM) samples were obtained from Alumina Corporation of China, located in Pingguo County, Guangxi Province, China. The raw red mud was dried in an oven at $105\text{ }^\circ\text{C}$ to remove the free water. Then, the dried red mud was filtered using a $74\text{-}\mu\text{m}$ mesh sieve to remove large quartz particles. The main components of the red mud were determined by X-ray fluorescence spectroscopy (XRF), and the test results are shown in Table 1.

Table 1. The main components of the red mud.

Compound	Fe_2O_3	Al_2O_3	CaO	Na_2O	SiO_2	TiO_2	SO_3	ZrO_2	K_2O
Mass percentage	27.95	23.36	16.58	8.05	14.93	6.21	0.771	0.364	0.344
Compound	Cr_2O_3	MgO	P_2O_5	V_2O_5	Cl	MnO	CeO_2	As_2O_3	Nb_2O_5
Mass percentage	0.322	0.244	0.236	0.131	0.104	0.0932	0.0687	0.0432	0.0411
Compound	ZnO	SrO	Sc_2O_3	PbO	NiO	CuO	WO_3	Ga_2O_3	Sum
Mass percentage	0.0131	0.0129	0.0121	0.0106	0.0093	0.0078	0.0061	0.0042	96.5

Analytically pure reagents sodium carbonate (Na_2CO_3 , 99.8%), calcium oxide (CaO , 99.9%), magnesium oxide (MgO , 99.9%), carbon dioxide (CO_2 , 99%), calcium sulfate (CaSO_4 , 99%) were purchased from Aladdin (Shanghai, China) and Damao-Reagent (Tianjin, China).

2.2. Methods

The flow chart of the entire experimental process is shown in Figure 1, the red mud and additives were homogeneously mixed in proportion by a grinder and calcined in a muffle furnace at different temperatures ($900\text{--}1150\text{ }^\circ\text{C}$) and durations (10–90 min). The samples were taken out and placed in the dryer for cooling down once the temperature fell below $650\text{ }^\circ\text{C}$. The addition process of magnesium oxide was as follows: the mass of CaO depended on the $\text{CaO}/(\text{SiO}_2 + \text{TiO}_2)$ molar ratio in the mixture (1.0, 1.6, 1.8, 2.0, 2.2, and 2.5); the mass of MgO depended on the $\text{MgO}/(\text{MgO} + \text{Fe}_2\text{O}_3)$ mass fraction in the spinel (13.04%, 14.89%, 16.67%, 18.37%, and 20%). All samples were prepared while keeping the constant Na/Al molar ratio at 1.2.

The leaching experiments were conducted in deionized water. First, the sintered samples were crushed and ground to a particle size $\leq 0.074\text{ mm}$ and were then leached in a water bath magnetic stirring kettle at different temperatures ($30\text{--}80\text{ }^\circ\text{C}$), durations (10–100 min), and L/S ratios (3:1–25:1). The leaching red mud and filtered solutions were later obtained by air pump filtration through a $0.45\text{-}\mu\text{m}$ mixed cellulose ester filter membrane. In this process, the dissolved rate of Al and Si was determined by measuring the contents of those elements in the leachate by using Inductively Couple Plasma optical

emission spectrometry method (ICP-OES). The leaching rates of Al and Si were calculated using Equation (1) as:

$$\eta = \frac{m}{m_{RM(Al,Si)}} \times 100\%, \quad (1)$$

where η (%) is the leaching rate of Al or Si, m is the content of alumina/silicon in the leachate (g), and $m_{RM(Al,Si)}$ is the content of alumina/silicon in the RM sample (g).

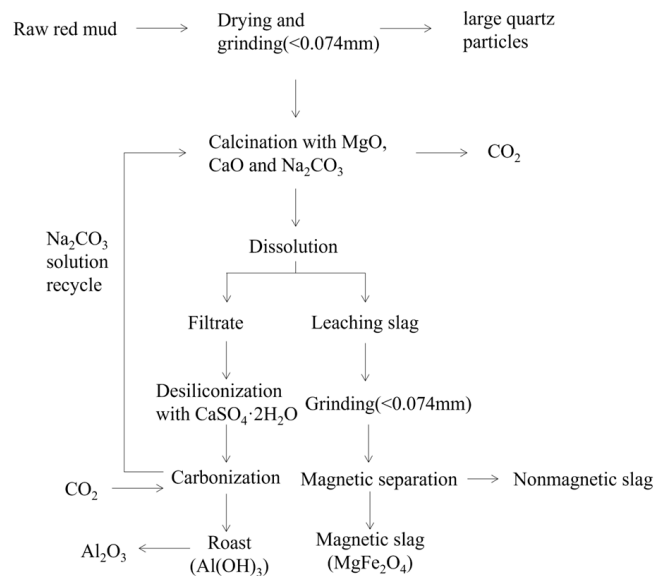
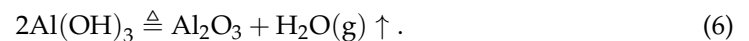
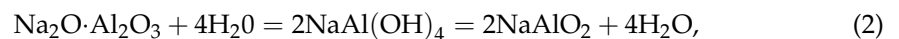


Figure 1. The flowchart of the magnetic sintering process.

According to a previous study [31], the slightly soluble CaSO_4 can be added for silica removal, carbonation, and solid roasting to recover calcium silicate, sodium carbonate, and high-purity alumina oxide, respectively. The reformed sodium carbonate can be recycled in the calcination process to reduce alkali consumption. The reactions occurred during the recovery of alumina and the recycling of filtrate were given in Equations (2)–(6) as follows:



The obtained leaching red mud was separated to obtain a magnetic concentrate in a wet magnetic separation tube at a magnetic induction of 50 mT, a working voltage of 220 V, and a working current of 0.15 A. The magnetic slag was treated by the wet digestion method ($\text{hClO}_4\text{-HNO}_3$). Then, the iron content was determined by the flame atomic absorption method (AAS). The recovery λ (%) of iron was calculated by Equation (7) as:

$$\lambda = \frac{m_{mag} \times \beta}{m_{RM} \times \alpha} \times 100\%, \quad (7)$$

where m_{mag} and m_{RM} are the masses of magnetic concentrate and raw red mud, respectively (g); and α and β are the iron grades of raw red mud and magnetic concentrate (magnetic slag), respectively.

2.3. Characterization

The corresponding oxide contents were determined using the ARL ADVAN[™]X Intellipower 3600 XRF with a divergence angle of 0.25°. For the mineralogical study, the Rigaku Ultima VI system X-ray diffractometer (XRD) was adopted in the powdered sample with Cu- α radiation and Ni-filter at the 2-Theta degree of 15°–85°, and the velocity was 5°/min.

The morphology and distribution were obtained using Scanning Electron Microscope (TESCAN MIRA LMS, Brno, Czech Republic) in the secondary electron (SE) mode. The samples were coated with a 10-mA platinum (Pt) layer to ensure the required conductivity before testing.

The concentrations of the elements in the leachate were measured using Fisher (iCAP 7200, Waltham, MA, USA) ICP-OES.

3. Results and Discussion

3.1. Characterization of Red Mud

From the XRD results shown in Figure 2, the diffraction pattern demonstrated heterogeneous peaks and complex mineral compositions that included hematite (Fe_2O_3), hydrogrossular ($\text{Ca}_3\text{Al}_2(\text{SiO}_4)_{3-x}(\text{OH})_{4x}$, $x > 1.5$), cancrinite ($\text{Na}_8(\text{AlSiO}_4)_6(\text{CO}_3)(\text{H}_2\text{O})_2$), Calcite (CaCO_3), Quartz (SiO_2), and Diaspore ($\text{AlO}(\text{OH})$). Iron was mostly found in hematite, with only a small amount of it distributed in silicates, carbonates, and sulfides. In addition, hydrogrossular and cancrinite were the primary sources of alumina and sodium in the experimental red mud, and these silicate minerals can hardly dissolve in the solution and only gradually release free calcium and sodium ions with time.

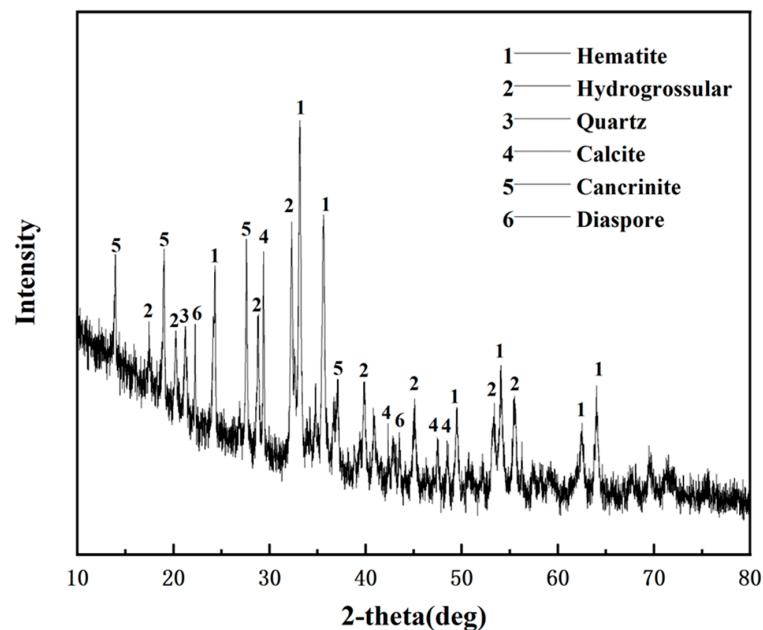


Figure 2. XRD pattern of the red mud sample.

Figure 3 illustrates the microstructure of the experimental red mud and the EDS analysis of the minerals, and the corresponding results are presented in Table 2. The red mud was composed of numerous aggregates formed by the accumulation of fine particles of different sizes and irregular shapes. Combined with the XRD and EDS analysis, bright particles (1) and crescent-like particles (3) correspond to hematite and cancrinite, whereas rod-like particles (2) correspond to cancrinite.

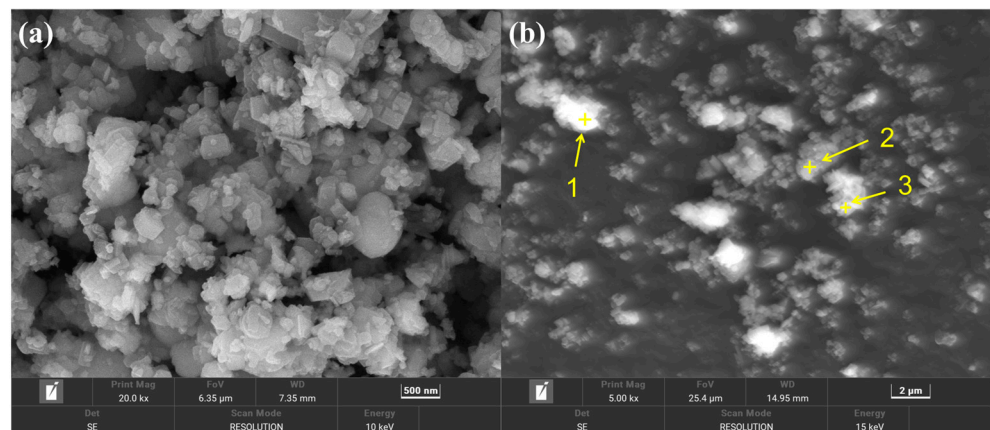


Figure 3. SEM image of red mud (a) and X-ray energy spectrum analysis of red mud (b) in the different points(1–3).

Table 2. EDS results of raw red mud corresponding to Figure 3b (in %).

Point	O	Na	Al	Si	Ca	Fe
1	53.58	8.42	5.91	4.09	0.71	27.30
2	60.51	13.02	11.12	10.55	1.01	3.79
3	63.43	4.31	3.08	2.07	0.65	24.46

3.2. Feasibility Analysis of $MgFe_2O_4$ Formation in the Sintering Process

3.2.1. Effect of Temperature on Sintering Behavior

The sintering temperature is one of the most significant factors in the phase transformation process. The macroscopic pictures of the sintering samples sintered at 1000–1150 °C (with the Ca/(Si + Ti) ratio of 1.8 and the MgO mass percentage in spinel of 14.89%) are presented in Figure 4. It can be directly seen that the sintered product became smaller and darker with all sintered materials being well attracted by the magnet, indicating that the sintering reaction became increasingly intense and the magnetic phase was formed between the Fe_2O_3 phase and MgO phase when the sintering temperature raised from 1000 °C to 1150 °C. Partial fusion occurred after the sintering temperature exceeded 1150 °C, and can be attributed to the melting point depression of the reaction system when the addition of sodium carbonate produced low melting point materials. A small amount of liquid phase accelerated the solid phase reaction, although too much liquid phase will lead to a dense sintered clinker that is unfavorable to crushing.

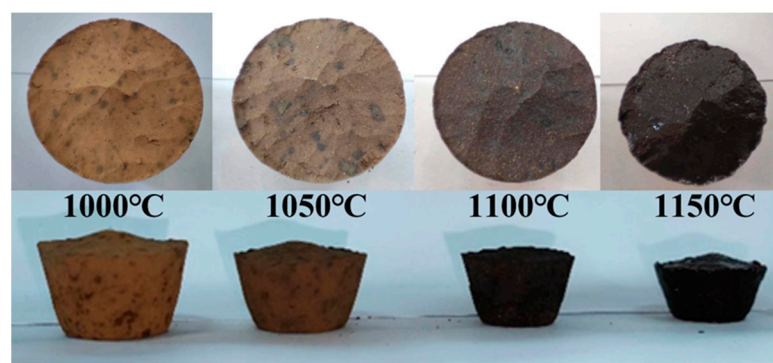


Figure 4. The macroscopic pictures of the sintering samples sintered at 1000–1150 °C (the Ca/(Si + Ti) ratio is 1.8 and MgO mass percentage in spinel is 14.89%).

3.2.2. Thermodynamic Trends in the Generation of Mineral Phases

The main reactions of clinker in the traditional soda-lime sintering process are: (1) Al_2O_3 and Na_2CO_3 generate sodium aluminate solid solution; (2) SiO_2 and CaO react to generate $2\text{CaO}\cdot\text{SiO}_2$; and (3) Fe_2O_3 and Na_2CO_3 generate sodium ferrate solid solution and when alkali dosage is insufficient and calcium oxide is present, the sodium ferrate further reacts to form calcium ferrate. This transversion can be completed within half an hour under $1200\text{ }^\circ\text{C}$. In addition, TiO_2 in red mud also reacts with CaO in the form of perovskite (CaTiO_3) at elevated temperatures. The formation and stability of magnesium ferrite based on the $\text{MgO}\text{-Fe}_2\text{O}_3$ binary system in the soda-lime sintering process are rarely reported [32].

A thermodynamic analysis of the reactions in which MgO may be involved was conducted to further study the reaction pattern after adding MgO to the sintering process [33–35]. The various reactions are listed in Table 3 in (1)–(5), along with the relationship between the Gibbs free energy (ΔG^0) calculated according to thermodynamic data and the temperature (HSC Chemistry) during their sintering in the standard state (Figure 5). The reaction between MgO and SiO_2 was spontaneous for all temperature conditions, which is not favorable to the formation of magnesioferrite (MgFe_2O_4). However, the formation of dicalcium silicate (Ca_2SiO_4) has significant precedence over the formation of magnesium silicate (Mg_2SiO_4), melilite ($\text{Ca}_2\text{MgSi}_2\text{O}_7$), and Diopside ($\text{CaMgSi}_2\text{O}_6$). When the calcium oxide content is sufficient, the magnetization reaction from MgO to MgFe_2O_4 in the sintering process is more significant than the formation of other magnesium-bearing compounds.

Table 3. Possible chemical reactions during the sintering process of red mud.

Reaction Number	Chemical Reaction
(1)	$2\text{CaO} + \text{MgO} + 2\text{SiO}_2 = \text{Ca}_2\text{MgSi}_2\text{O}_7$
(2)	$\text{MgO} + \text{Fe}_2\text{O}_3 = \text{MgFe}_2\text{O}_4$
(3)	$2\text{MgO} + \text{SiO}_2 = \text{Mg}_2\text{SiO}_4$
(4)	$\text{MgO} + \text{CaO} + 2\text{SiO}_2 = \text{CaMgSi}_2\text{O}_6$
(5)	$2\text{CaO} + \text{SiO}_2 = \text{Ca}_2\text{SiO}_4$
(6)	$\text{Fe}_2\text{O}_3 + \text{Na}_2\text{CO}_3 = 2\text{NaFeO}_2 + \text{CO}_2\text{ (g)}$
(7)	$\text{Fe}_2\text{O}_3 + \text{CaO} = \text{CaO}\cdot\text{Fe}_2\text{O}_3$
(8)	$\text{Fe}_2\text{O}_3 + 2\text{CaO} = 2\text{CaO}\cdot\text{Fe}_2\text{O}_3$
(9)	$2\text{CaO}\cdot\text{Fe}_2\text{O}_3 + 2\text{MgO} + \text{SiO}_2 = 2\text{MgFe}_2\text{O}_4 + \text{Ca}_2\text{SiO}_4$
(10)	$2\text{CaO}\cdot\text{Fe}_2\text{O}_3 + \text{MgO} + \text{SiO}_2 = \text{MgFe}_2\text{O}_4 + \text{Ca}_2\text{SiO}_4$

The formation of calcium ferrate and sodium ferrate is typical in the lime soda method of red mud. Once these reactions occur, impurities such as iron oxide and calcium ferrate will appear in the leaching slag, which is detrimental to the separation of iron. The thermodynamic calculations of reactions (6)–(8) in the standard state are plotted in Figure 6. The formation of $2\text{CaO}\cdot\text{Fe}_2\text{O}_3$ and $\text{CaO}\cdot\text{Fe}_2\text{O}_3$ was superior to that of $\text{Na}_2\text{O}\cdot\text{Fe}_2\text{O}_3$ under the experimental conditions. The formed low-magnetic calcium ferrates could stabilize a part of the free calcium in the system during the sintering process, but they also consumed some iron oxide. According to reactions (9)–(10), the results of the mutual reactions eventually pointed to the formation of magnesioferrite and dicalcium silicate. The value of ΔG^0 of the ferrite substitution reactions was negative, indicating that the magnetization reaction from Fe_2O_3 to MgFe_2O_4 spinel can proceed under normal sintering conditions.

According to the binary phase diagram of $\text{Fe}_2\text{O}_3\text{-MgO}$ with high-temperature calcination in air ($P(\text{O}_2) = 0.21\text{ atm}$) in Figure 7. The dashed line represents the equilibrium phase for different MgO contents at 1373 K . The low MgO contents caused the precipitation of Fe_2O_3 in decreasing temperatures (Point A). For pure MgFe_2O_4 , the mass fractions of MgO and Fe_2O_3 are 20.15% and 79.85%, respectively, corresponding to a mixture fraction of MgFe_2O_4 and MgO (Point B) that not only consumes excessive MgO but also has a negative effect on the separation of magnetic minerals from the mixture. Theoretically, the mass fraction of the magnesium oxide that only forms MgFe_2O_4 is in the range of

16.8%–19.87%. Based on the above analysis, the experimental mass fraction of MgO in spinel was controlled at 13.04% to 20%.

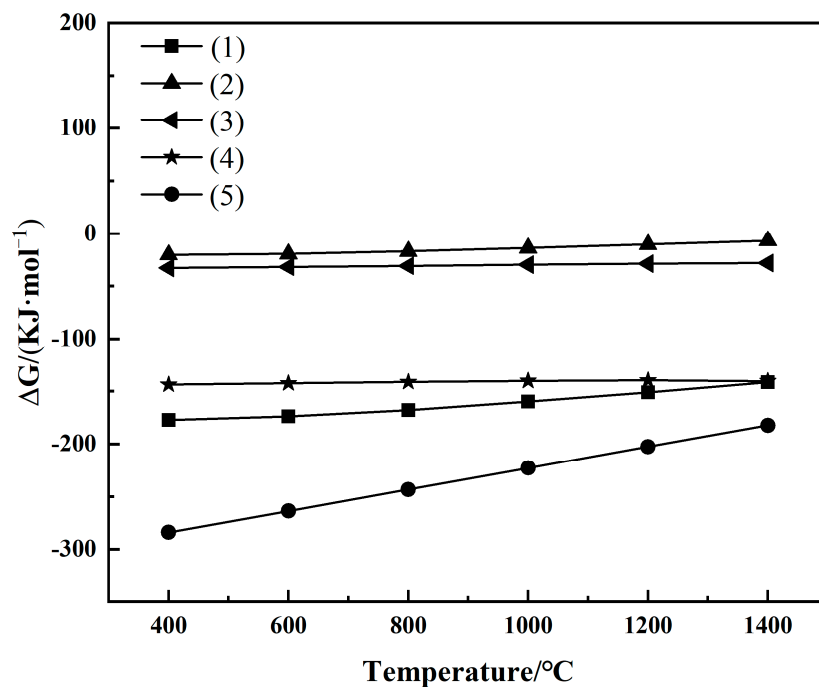


Figure 5. Correlation between the standard Gibbs free energy (ΔG^\ominus) and temperature for reactions (1)–(5) in Table 3.

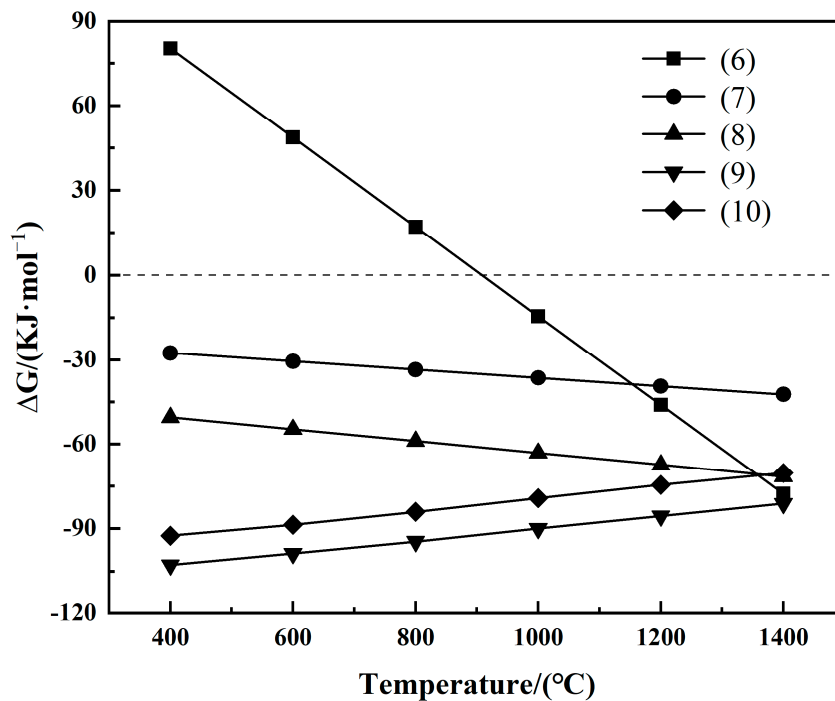


Figure 6. Correlation between the standard Gibbs free energy (ΔG^\ominus) and temperature for reactions (6)–(10) in Table 3.

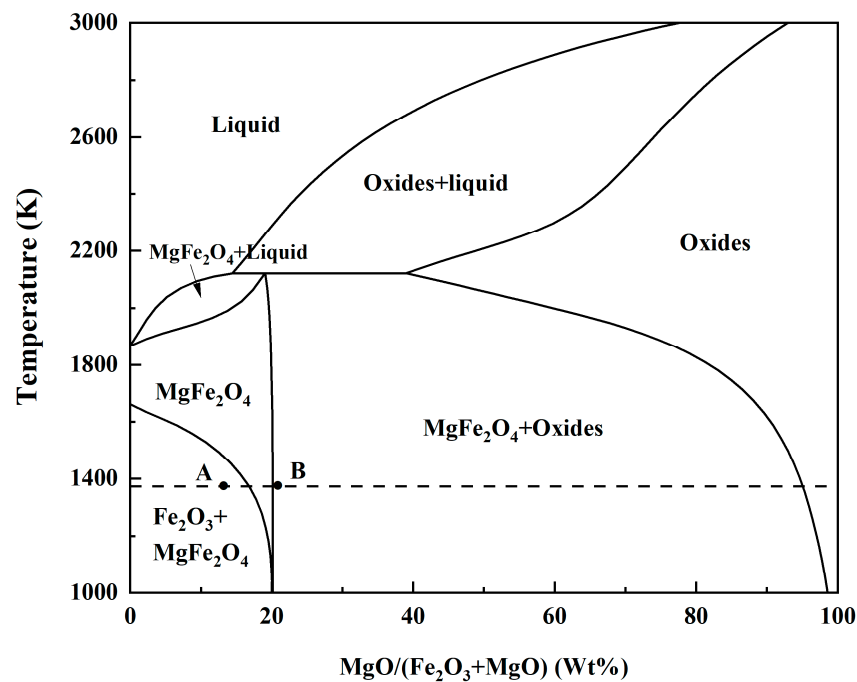


Figure 7. Phase diagram of Fe_2O_3 - MgO in air ($P(\text{O}_2) = 0.21 \text{ atm}$). Point A: The composition of the sintered product under a low MgO content; Point B: The composition of sintered products under pure MgFe_2O_4 spinel conditions.

3.3. The Formation of Phase in Sintered Product under Different Roasting Parameters

3.3.1. Temperature

The XRD analysis of the sintering samples at different temperatures (the $\text{Ca}/(\text{Si} + \text{Ti})$ molar ratio was 1.6 and the MgO mass fraction was 20.0%) are depicted in Figure 8. The diffraction peaks of PDF#88-1935 in the card database (jade 6.5) and MgFe_2O_4 in the sintering products corresponded well to the diffraction angle and height. This indicated that MgFe_2O_4 of clinker was formed by solid phase reaction at different temperatures. However, the impurity composition of red mud and different temperatures affected its phase content, as verified in the XRD pattern at low temperatures. Impurity minerals such as $\text{Ca}_3\text{Al}_2(\text{O}_4\text{D}_4)_3$, $\text{Ca}_2\text{Fe}_2\text{O}_5$, and Al_2SiO_5 were observed at 900°C , indicating that the reaction between magnesium oxide and iron oxide was less advantageous than the side reaction between iron oxide and other oxides at lower temperatures. With the increase of the roasting temperature, these impurity phases gradually disappeared or weakened. The $\text{Ca}_2\text{Fe}_2\text{O}_5$ phase was hard to detect at 1150°C , whereas the diffraction intensity of MgFe_2O_4 increased to the maximum. Another essential phase for the dissolution of alumina, i.e., sodium aluminate, was mainly generated from 1000 to 1100°C . The small change in the intensity of the sodium aluminate diffraction peak may be due to the low content of calcium oxide, which led to incomplete consumption of the silicate in the system. CaO reacted with silica to produce insoluble substances ($\beta\text{-Ca}_2\text{SiO}_4$) and prevent the reaction of silicon and sodium aluminate. After the temperature exceeded 1000°C , the phase composition remained unchanged, and the main phases were MgFe_2O_4 , CaTiO_3 , Ca_2SiO_4 , NaAlO_2 , $\text{Ca}_2\text{Fe}_2\text{O}_5$, and $\text{Ca}_3\text{Al}_2\text{O}_6$.

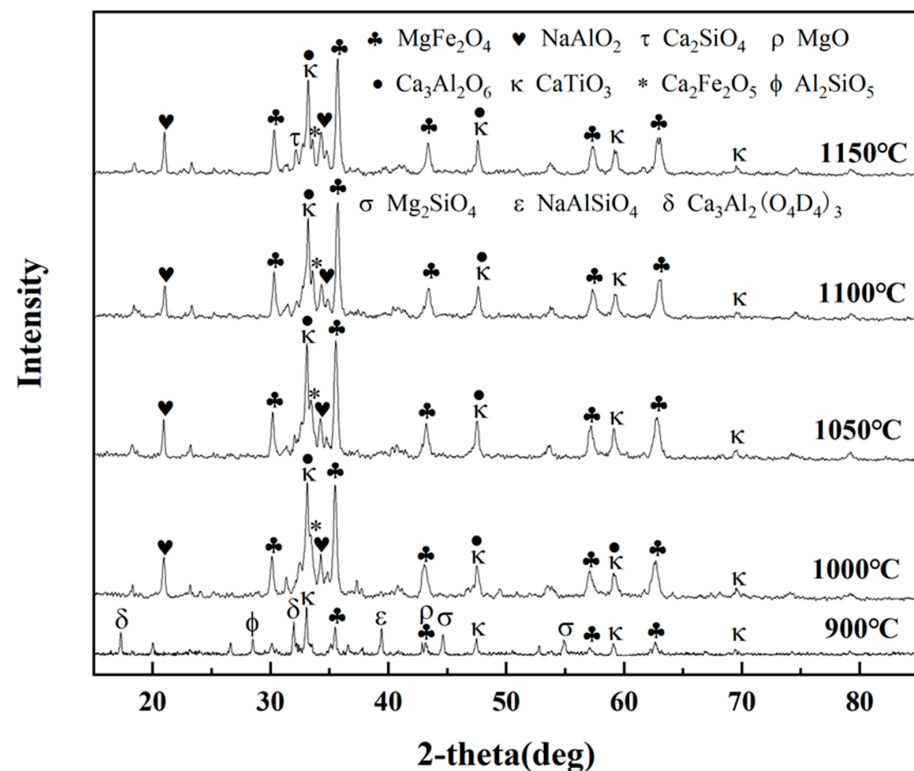


Figure 8. XRD patterns of the sintered red mud at different sintering temperatures.

3.3.2. Time

Figure 9 illustrates the XRD patterns at 1100 °C at different sintering times (with the Ca/(Si + Ti) molar ratio at 1.8 and the MgO mass fraction at 20.0%). From the figure, the MgFe_2O_4 spinel phase and NaAlO_2 phase were found in all sintered samples. When the sintered time was 15 min, these phases had formed while the sodium silicon aluminate phase was not detected, indicating that the chemical reaction between the compounds had preferable kinetic conditions and fast reaction rates. With a longer sintered time, the height of the formed MgFe_2O_4 spinel diffraction peaks gradually increased (from 110 at 15 min to 128 at 90 min), indicating that the solid phase reaction of MgFe_2O_4 spinel could not reach equilibrium under the experimental conditions, and its content was still increasing. However, for the NaAlO_2 phase, there were no significant changes observed between 60 and 90 min, but an increase in the phase diffraction intensity from 30 to 60 min. When the sintering time was 90 min, a better Ca_2SiO_4 phase can be formed with the calcium oxide molar ratio was at 1.8 than at 1.6 (Figure 8), indicating that a calcium oxide molar ratio of 1.8 had a propitious phase to extract alumina.

3.3.3. The Effect of MgO on Sintering Samples

Figure 10 shows the XRD patterns of samples with different MgO mass fractions when the C/(S + T) ratio was 2.0 at 1100 °C and the magnified image at the spinel diffraction peak of around 35.5°. The spinel peak strength was relatively low when the MgO mass fraction was 13.04%, a low-magnesium spinel ($(\text{Mg}^{2+}, \text{Fe}^{2+})\text{Fe}_2\text{O}_4$) may be formed. It can be explained that the partial reduction of the Fe_2O_3 in the $\text{MgO-Fe}_2\text{O}_3\text{-MgFe}_2\text{O}_4$ system at experimental temperature was found to meet the material equilibrium [36]. When the MgO content was 16.67%, the spinel phase agreed well with MgFe_2O_4 in PDF#88-1935. However, a shift in the spinel diffraction angle (from 35.49° at 16.67% to 35.55° at 20%) was observed when the MgO content continually increased to 18.37% and then to 20.0%. The spinel diffraction peak at this condition was close to the $\text{MgAl}_{0.2}\text{Fe}_{1.98}\text{O}_4$ diffraction peak. A small number of periclase (MgO) peaks appeared (Figure 10a), indicating that the magnesioferrite spinel formation reaction at the experimental condition might be

incomplete. O'Neill et al. [37] argued that magnesioferrite is possibly stoichiometric at low temperatures, and nonstoichiometric magnesioferrite can be generated at a relatively high temperature (>1000 °C). The case that diffraction peaks shifted to higher angles could be explained by the lattice defects caused by the excessive MgO or Al₂O₃ dissolved in the magnesioferrite spinel lattice. Dieckmann and Schmalzried [38,39] showed that the formation of magnesioferrite is mainly due to the mobility of a kind of cations rather than oxygen vacancy. The ionic radii of Mg²⁺ (0.66 Å), Fe²⁺ (0.74 Å), Fe³⁺ (0.64 Å), and Al³⁺ (0.51 Å) are similar. Therefore, Fe³⁺ and Fe²⁺ can be easily substituted by Mg²⁺ and Al³⁺. The intensity and angle of the diffraction peaks of Ca₂SiO₄ in different MgO contents hardly changed, indicating that MgO did not react with Ca₂SiO₄ when calcium oxide content was in a certain range, which is consistent with the previous thermodynamic analysis.

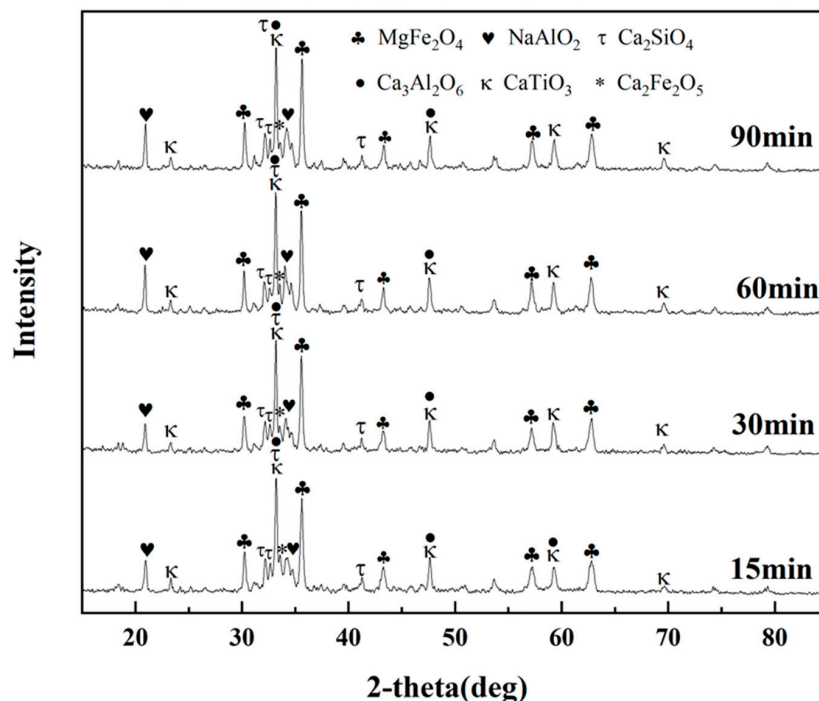


Figure 9. XRD patterns of the sintered red mud at different times.

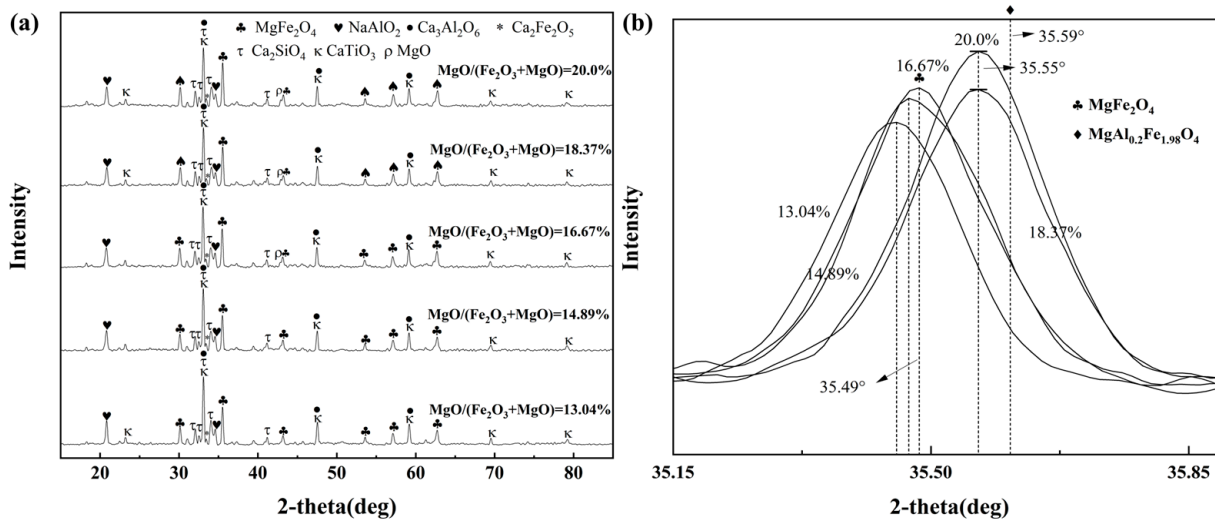


Figure 10. XRD patterns of the sintered red mud with different MgO mass fractions (a) and magnified image at the spinel diffraction peak (b).

3.4. Recovery Efficiencies of Alumina from Red Mud

The XRD pattern showed good intensity for MgFe_2O_4 spinel diffraction peaks, but the intensity for sodium aluminate was not obvious. In this section, the single-factor approach was continued to be applied to examine several key factors that affected alumina extraction rate, including temperature, MgO mass fraction, C/(S + T) molar ratio, leaching temperature, leaching time, and liquid/solid ratio (L/S in ml/g). Furthermore, the behavior of the silicon dissolution of clinker during the leaching process was also studied to improve the purity of sodium aluminate in the leachate.

3.4.1. Effect of Calcination Conditions on Alumina Extraction

Experiments were conducted under the following leaching parameters: leaching temperature: 60 °C; leaching time: 20 min; and liquid/solid (L/S) ratio: 10:1.

The alumina dissolution rate at different roasting temperatures (the Ca/(Si + Ti) ratio was 1.8 and the MgO mass fraction was 16.67%) is shown in Figure 11a. The alumina dissolution rate (72.07%) at 1100 °C was the highest. With the roasting temperature increased to 1150 °C, the sintered material may produce a glassy phase in which the alumina was encapsulated to reduce the extraction efficiency [40]. The most significant variation in the extraction rate occurred at a temperature of 1000 °C, with a consistent increase in the alumina extraction rate in the range of 1000–1100 °C. These results might suggest that a calcination temperature of 1100.0 °C could lead to optimal sintered material that is favorable for the extraction of alumina, compared to other temperatures. The variation also indicated that a temperature of 1000 °C mainly lead to the production of a beneficial mineralogical phase (NaAlO_2), in which sodium carbonate reacted with alumina oxides rather than further generating NaAlSiO_4 with silicon at lower temperatures (900 °C). NaAlSiO_4 can hardly dissolve in the solution, which could be the main reason for the lower alumina extraction rate at low temperatures.

Figure 11b illustrates the alumina extraction rate with different MgO contents under the experimental conditions (1100 °C with the Ca/(Si + Ti) ratio at 1.8). The rate had no significant difference ranging from 70.5% to 72.4% with an overall decreasing trend, corresponding to the magnesium oxide content from 13.04% to 20%, which might be attributed to the re-reaction of the incomplete reaction of excessive MgO with NaAlO_2 to form precipitates during the leaching process.

Figure 11c demonstrates the effect of different Ca/(Si + Ti) ratios (1100 °C with the MgO mass fraction at 16.67%) on alumina extraction. The alumina leaching rate had a significant enhancement when the Ca/(Si + Ti) ratio increased from 1.0 to 1.8 because CaO played a role in preventing the high activity of SiO_2 from affecting alumina leaching. When the Ca/(Si + Ti) ratio exceeded 1.8, not only the alumina leaching rate gradually decreased, but also it resulted in the generation of many impurities, such as $\text{Ca}_2\text{Fe}_2\text{O}_5$, $\text{Ca}_3\text{Mg}(\text{SiO}_4)_2$, and $3\text{CaO}\cdot\text{SiO}_2$. More SiO_2 was available to form soluble silicate in the leaching process, causing a possible decline in the purity of sodium aluminate in the solution.

3.4.2. Effect of Leaching Conditions on Alumina Extraction

The leaching experiments were performed under a temperature of 1100 °C, a MgO content of 16.67%, and a Ca/(Si + Ti) ratio of 1.8.

Figure 12a depicts the dissolution rates of Al and Si in the different leaching temperatures with a leaching time of 20 min and an L/S ratio of 10:1. The extraction rate of Al gradually increased with the increase of temperature and reached the equilibrium at 60 °C. The dissolution rate of Si also gradually increased, and this trend was enhanced at higher temperatures (>70 °C). Since the dissolution reaction of Si and Al was exothermic ($\Delta H < 0$), the Gibbs free energy was negative ($\Delta G < 0$), indicating that the rise of temperature will promote the reaction to a certain degree. In general, the leaching reaction of alumina in this process was more evident at 60 °C than at other temperatures.

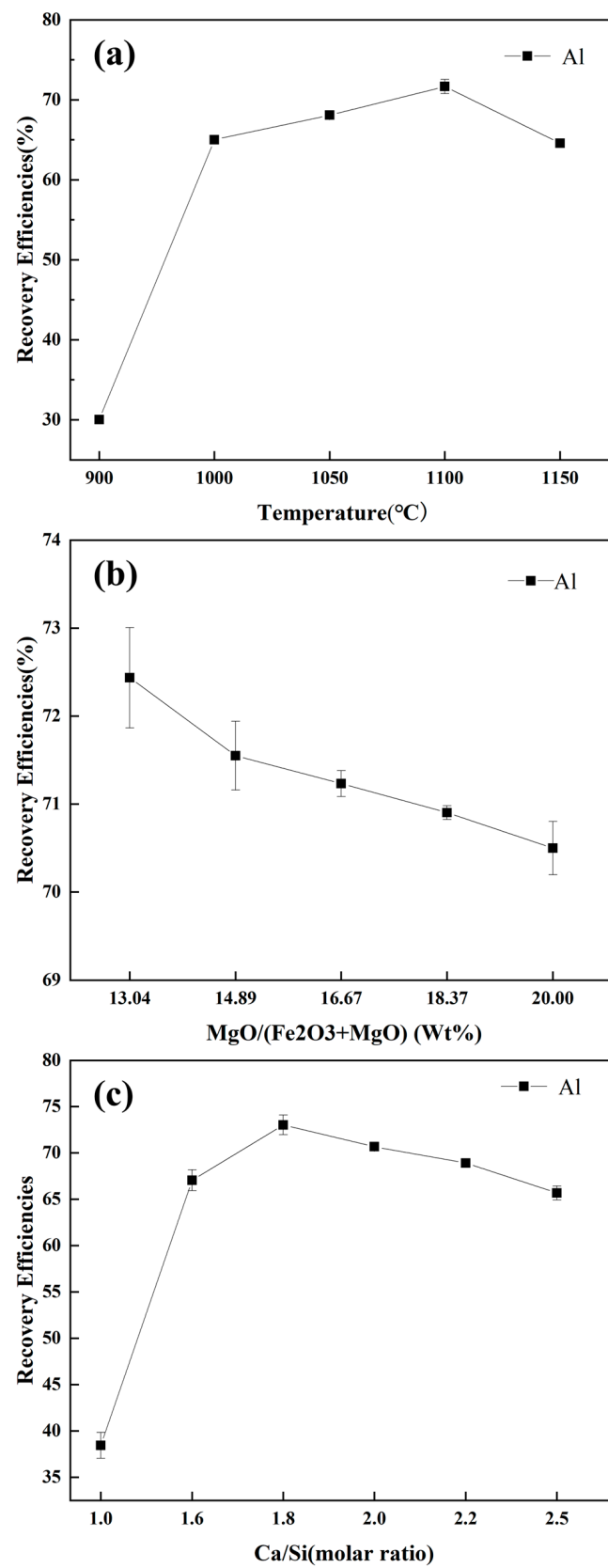


Figure 11. Recovery efficiency of alumina under different sintering conditions: calcination temperature (a), MgO/(Fe₂O₃ + MgO) ratio (b), and Ca/(Si + Ti) ratio (c).

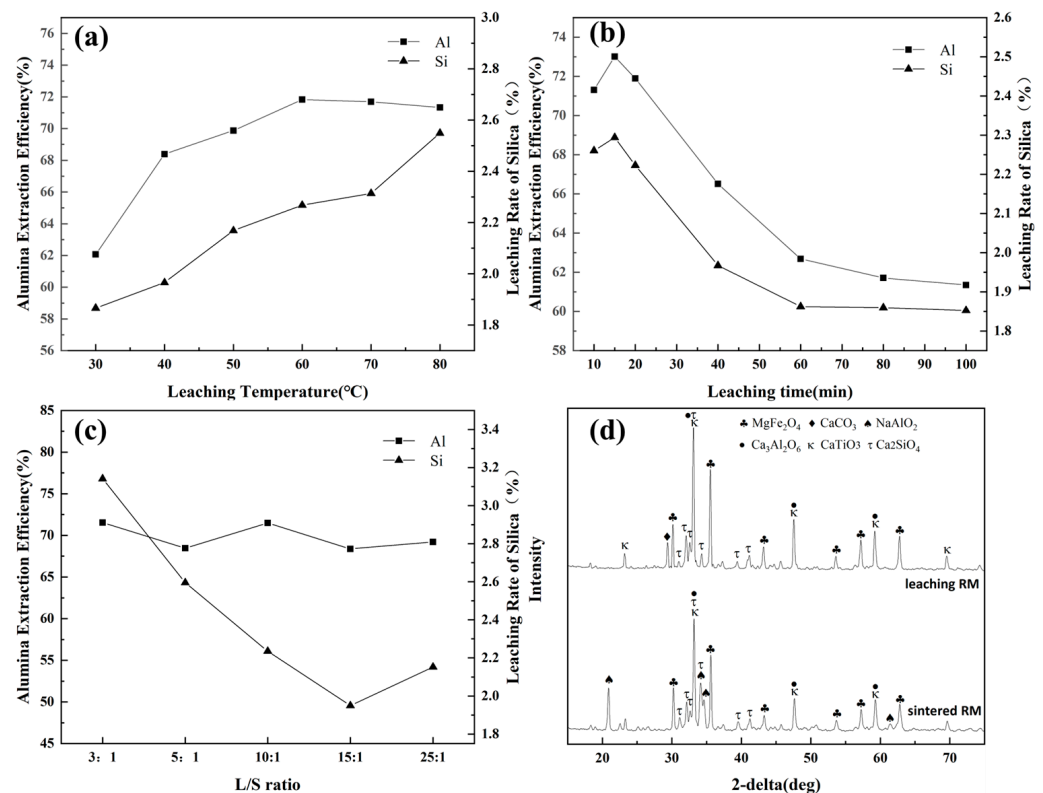


Figure 12. The dissolution rates of Al and Si in different leaching conditions: leaching temperature (a), leaching time (b), and the leaching liquid/solid (L/S) ratio (c); and the XRD patterns of the sintered red mud and leaching red mud (d).

Figure 12b demonstrates the extraction results when the temperature was 60 °C and the L/S ratio was 10:1. There were 73.1% of Al and 2.3% of Si dissolved from the sintering sample within 15 min. However, the recovery fell with a prolonged leaching time, which may be contributed to the secondary reaction, where NaAl(OH)_4 , Ca^{2+} , and SiO_4^{2-} produced precipitates of $[\text{Na}_2\text{O} \cdot \text{Al}_2\text{O}_3 \cdot 2\text{SiO}_2] \cdot \text{NaAl(OH)}_{6-n} \cdot \text{H}_2\text{O}$ and $3\text{CaO} \cdot \text{Al}_2\text{O}_3 \cdot n\text{SiO}_2 \cdot (6 - 2n) \cdot \text{H}_2\text{O}$. Specifically, calcium sulfate was added in this process to initiate the reaction of silicate ions with calcium ions and generate calcium silicate precipitates, which is different from traditional desilication methods that use CaO or Ca(OH)_2 [41]. The slightly soluble calcium sulfate can provide a low level of Ca^{2+} ions to avoid excessive consumption of alumina (AlO_2^-) in the solution.

Figure 12c shows the leaching results for different L/S ratios at 60 °C and 20 min. The extraction rate of Al at different L/S ratios hardly changed because the solubility of sodium aluminate was exceptionally large in water. By contrast, the dissolved arrival rate of silicon decreased at large L/S ratios, due probably to the high mass concentration of sodium aluminate interacting with the insoluble Ca_2SiO_4 to cause the decomposition of calcium silicate [42]. Therefore, the L/S ratio may not be the main factor affecting the dissolution of Al in this experiment, and increasing the liquid/solid (L/S) ratio might decrease the dissolution of silicate in a certain range.

The XRD patterns of the leaching red mud and sintered red mud are illustrated in Figure 12d. The disappearance of the sodium aluminate phase after the leaching process was accompanied by the enhancement of diffraction peaks of other phases, indicating that the content in the leaching residue was enhanced. The partial weakening of the Ca_2SiO_4 peak and the appearance of the CaCO_3 peak were also observed because the calcium ions dissolved from calcium silicate reacted with carbon dioxide in the air under the stirring effect of the leaching process.

3.5. Microstructural Studies

The morphology and EDS results of the sintered red mud with MgO (with a MgO content of 16.67%) and CaO (the Ca/(Si + Ti) molar ratio was 1.8), and its leaching red mud and magnetic separation product sintered at 1100 °C for 90 min are shown in Figures 13 and 14. The SEM images of the sintered material are obtained with magnifications from 500× to 5k×. On the one hand, the original red mud mainly consisted of irregular particles in very small agglomerates (Figure 3a), which contained various impurities. In contrast, the sintered materials crystallized extensively with each other to form larger particles, indicating good sintering conducive to the separation of Fe-bearing materials. On the other hand, the particles also showed a crack structure, the production of this structure may be related to the decomposition of the added carbonate that produced gas, and the crack structure increased the specific surface area of the particles, which supplied a good solid-liquid reaction basis for the later leaching process. Combining the EDS results (Table 4) and XRD analysis, the mineral phase of the sintered red mud, leaching red mud and magnetic separation production mainly consisted of NaAlO_2 , MgFe_2O_4 , C_2S , and C_2F . NaAlO_2 contained a small amount of silicon and iron. MgFe_2O_4 was mixed with alumina and calcium, in which the Mg/Fe ratio was 0.4677–0.528, which is slightly different from that of the standard MgFe_2O_4 of 0.5. The Ca/Si ratio of C_2S particles and the Ca/Fe ratio of C_2F particles were close to 2.0 and 1.0, respectively, showing good elemental analyticity.

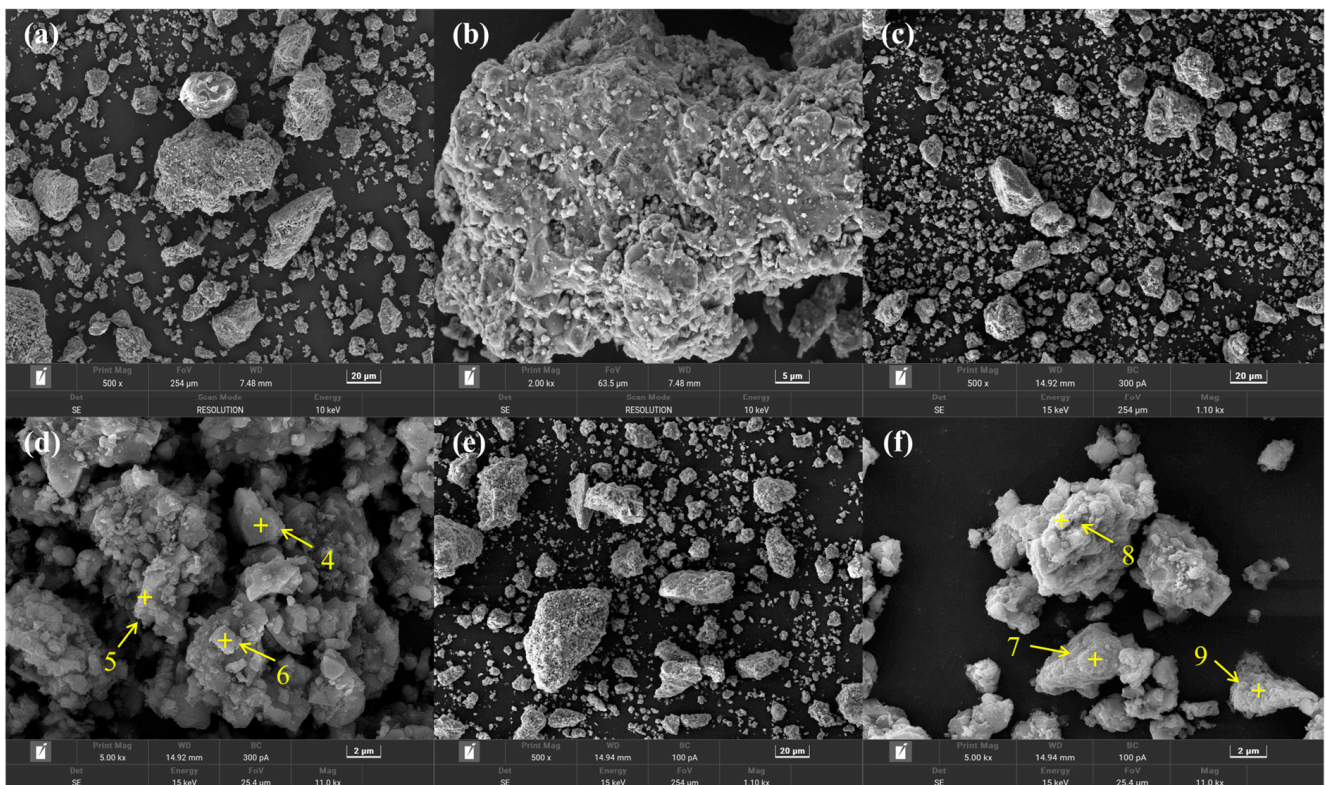


Figure 13. SEM images of the sintered red mud (a,b); leaching red mud (c,d); and magnetic separation product(e,f) with magnifications from 500× to 5k×; The yellow numbers (4–9) in the subfigures (d,f) corresponding to the EDS results in the Table 4.

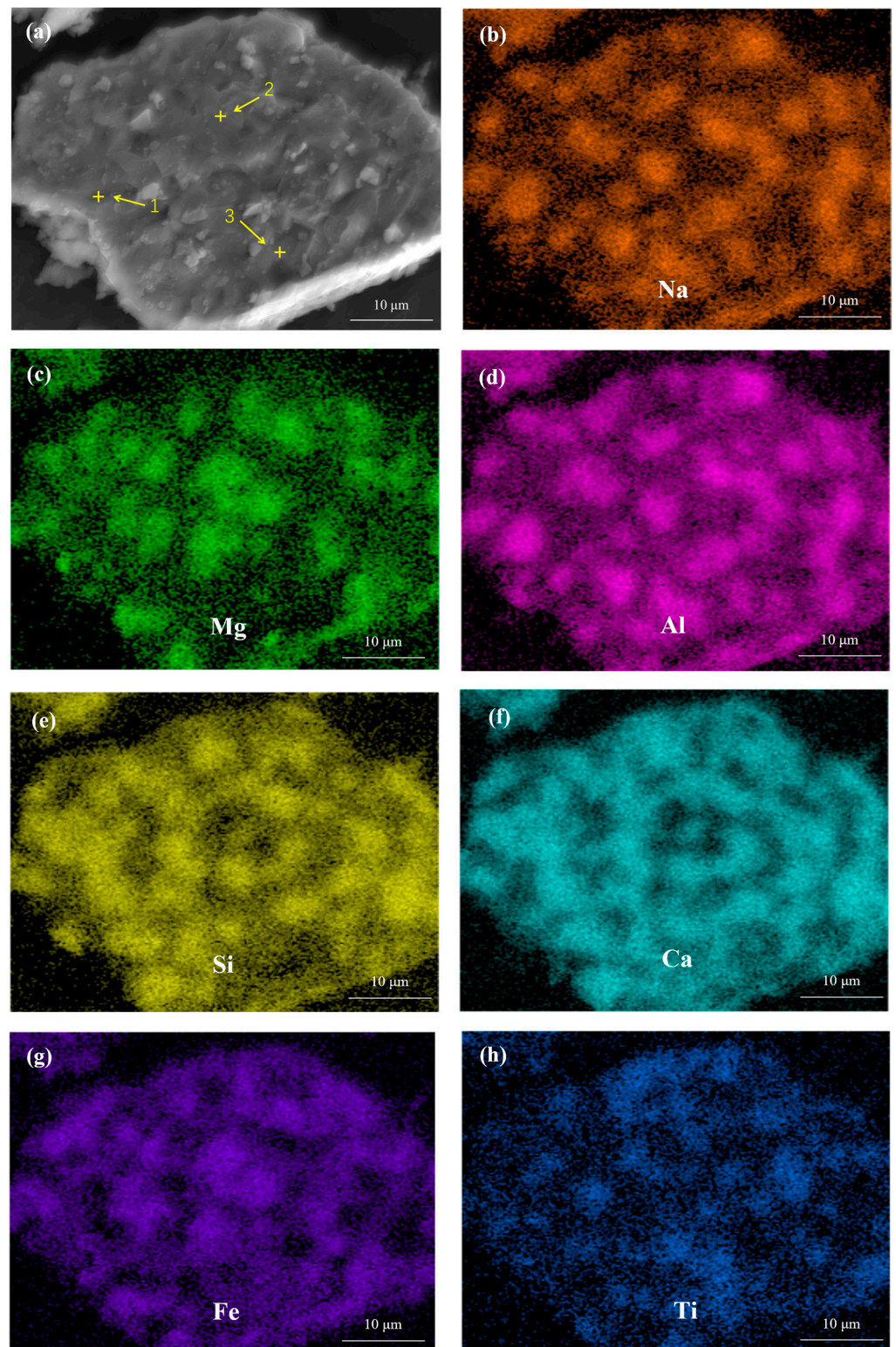


Figure 14. The yellow numbers (1–3) in the subfigure (a) corresponding to the EDS results in the Table 4; X-ray energy spectrum analysis and elemental distribution of the Na (b), Mg (c), Al (d), Si (e), Ca (f), Fe (g) and Ti (h) in the sintered red mud.

Table 4. EDS results of different points (1–9) corresponding to those in Figures 13a and 12d,f (in %).

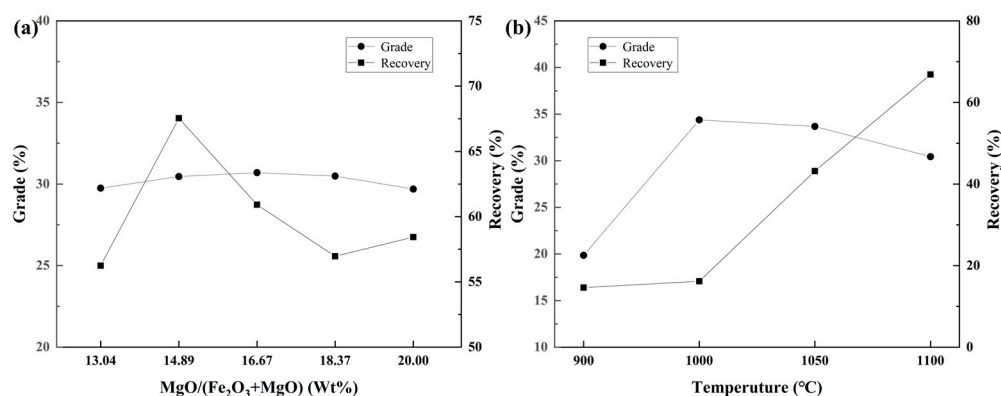
Point	Mineral Phases	O	Na	Mg	Al	Si	Ca	Ti	Fe
1	NaAlO ₂	52.13	22.28	0.15	16.91	2.44	1.41	0.41	4.26
2	MgFe ₂ O ₄	47.23	1.42	13.30	4.60	1.16	3.42	0.42	28.44
3	C ₂ S	63.11	3.00	0.24	1.58	10.00	19.87	0.81	1.4
4	C ₂ F	57.89	1.32	0.34	2.18	1.25	18.48	0.97	17.56
5	C ₂ S	68.59	0.62	0.39	0.81	9.72	17.78	0.40	1.70
6	MgFe ₂ O ₄	58.74	0.15	11.55	2.90	1.24	2.49	0.37	22.55
7	CaCO ₃	71.80	0.13	0.64	0.72	1.14	22.07	0.96	2.64
8	MgFe ₂ O ₄	59.13	0.32	10.70	2.62	1.60	4.45	0.93	20.26
9	MgFe ₂ O ₄	56.70	0.54	11.89	2.11	1.93	2.82	2.42	22.58

3.6. Magnetic Separation of Iron from Leaching Red Mud

The magnetic separation results of the leaching red mud are shown in Table 5 and Figure 15. The total iron grade and recovery rate of the magnetic slag were 30.46% and 67.54%, respectively, under a MgO content of 14.89% and a temperature of 1100 °C. The total Fe grade of the magnetic slag increased by 13.68% compared to that of raw red mud (17.28%). Moreover, some researchers performed direct magnetic recovery of iron from red mud without any treatment. The recovery rate was only 25% and the total Fe grade of magnetic slag increased by about 10%, indicating unsatisfactory results. After separation, the residual slag can produce high-value-added construction materials or heavy metal adsorption materials in the environmental field due to its lower Na content at about 0.61%. The result of this study is helpful to significantly improve alumina recovery and vastly reduce the amount of red mud generated in the refineries, and the technology is promotional for the comprehensive utilization of red mud and iron production.

Table 5. The grade and recovery of the de-alkalized red mud at 50 mT.

Sample	MgO/(Fe ₂ O ₃ + MgO) (wt%)					Temperature (°C)			
	13.04	14.89	16.67	18.37	20.0	900	1000	1050	1100
Grade (%)	29.75	30.46	30.70	30.49	29.69	19.86	34.38	33.68	29.43
Recovery (%)	56.24	67.54	60.92	56.96	58.43	14.60	16.18	43.18	66.85

**Figure 15.** The grade and recovery of the de-alkalized red mud at 50 mT in different MgO/(Fe₂O₃+MgO) mass fraction (a) and temperature (b).

4. Conclusions

A new magnetization process that included magnetization sintering, atmospheric-pressure leaching, and magnetic separation was proposed to comprehensively utilize iron-bearing red mud. According to the experimental results, the conclusions can be drawn as follows: (1) The generation of MgFe₂O₄ and NaAlO₂ phases was closely related to the sintering temperature. The optimal sintering temperature was 1100 °C, and the main phases were MgFe₂O₄, CaTiO₃, Ca₂SiO₄, NaAlO₂, Ca₂Fe₂O₅, and Ca₃Al₂O₆; (2) The for-

mation of MgFe_2O_4 spinel had a higher iron recovery rate when the $\text{MgO}/(\text{Fe}_2\text{O}_3 + \text{MgO})$ mass fraction was 14.89% (corresponding to Fe recovery and grade are 67.94% and 30.46%, respectively), as the forming reaction between Fe_2O_3 and MgO is nonstoichiometric at relatively elevated temperatures; (3) The addition of CaO within a certain range can reduce the thermodynamic activity of SiO_2 in the reactants while facilitating the extraction of Al from the roasting products; (4) The leaching temperature and time of solution have greater significance than the L/S ratio in the dissolution of Al and Si from the sintering material, and 73.1% of Al and 2.3% of Si were dissolved under the optimal condition; and (5) the obtained Mg/Fe ratio of the magnetic separation product was in a range of 0.4677–0.528, which is slightly different from that of the standard MgFe_2O_4 at 0.5.

Author Contributions: Conceptualization, R.C. and L.S.; Data curation, R.C.; Funding acquisition, H.H.; Investigation, R.C. and J.Y.; Project administration, H.H.; Supervision, L.S.; Validation, R.C. and H.H.; Visualization, R.C. and J.Y.; Writing—original draft, R.C.; Writing—review & editing, R.C. and L.S. All authors have read and agreed to the published version of the manuscript.

Funding: This work was supported financially by the Social Public Welfare and Basic Research Project of Zhongshan City [No. 2020B2004] and Key Research and Development Program of Guangzhou City [No. 202206010053].

Data Availability Statement: The data presented in this study are available on request from the corresponding author.

Conflicts of Interest: The authors declare that they have no known competing financial interests or personal relationships that could have appeared to influence the work reported in this paper.

References

1. Economou-Eliopoulos, M. Potential leaching of Cr(VI) from laterite mines and residues of metallurgical products (red mud and slag): An integrated approach. *J. Geochem. Explor.* **2016**, *162*, 40–49. [[CrossRef](#)]
2. Agrawal, S.; Dhawan, N. Evaluation of red mud as a polymetallic source—A review. *Miner. Eng.* **2021**, *171*, 107084. [[CrossRef](#)]
3. Hadji, R.; Boumazbeur, A.E.; Limani, Y.; Baghem, M.; Chouabi, A.E.M.; Demdoum, A. Geologic, topographic and climatic controls in landslide hazard assessment using GIS modeling: A case study of Souk Ahras region, NE Algeria. *Quat. Int.* **2013**, *302*, 224–237. [[CrossRef](#)]
4. Zhang, T.A.; Wang, K.; Liu, Y.; Lyu, G.Z.; Li, X.F.; Chen, X. A Review of Comprehensive Utilization of High-Iron Red Mud of China. In Proceedings of the Light Metals Symposia at the 149th The-Minerals-Metals-and-Materials-Society (TMS) Annual Meeting and Exhibition, San Diego, CA, USA, 23–27 February 2020; Springer International Publishing Ag: San Diego, CA, USA, 2020; pp. 65–71.
5. Chen, X.; Guo, Y.; Ding, S.; Zhang, H.; Xia, F.; Wang, J.; Zhou, M. Utilization of red mud in geopolymer-based pervious concrete with function of adsorption of heavy metal ions. *J. Clean. Prod.* **2019**, *207*, 789–800. [[CrossRef](#)]
6. Mukiza, E.; Zhang, L.; Liu, X.; Zhang, N. Utilization of red mud in road base and subgrade materials: A review. *Resour. Conserv. Recycl.* **2019**, *141*, 187–199. [[CrossRef](#)]
7. Ahmadi, H.; Khalaj, G.; Najafi, A.; Abbasi, S.M.; Safari, M. Metakaolin-red mud/carbon nanotubes geopolymer nanocomposite: Mechanical properties and structural studies. *Mater. Res. Express* **2022**, *9*, 025011. [[CrossRef](#)]
8. Wang, M.; Liu, X. Applications of red mud as an environmental remediation material: A review. *J. Hazard. Mater.* **2021**, *408*, 124420. [[CrossRef](#)]
9. Luo, H.-L.; Huang, S.-S.; Luo, L.; Liu, Y.; Tian, J. In-situ stabilization remediation of lead contaminated soil by application of red mud based particles. *J. Cent. South Univ.* **2011**, *42*, 1819–1824.
10. Liu, Q.; Xin, R.; Li, C.; Xu, C.; Yang, J. Application of red mud as a basic catalyst for biodiesel production. *J. Environ. Sci.* **2013**, *25*, 823–829. [[CrossRef](#)]
11. Sushil, S.; Batra, V.S. Catalytic applications of red mud, an aluminium industry waste: A review. *Appl. Catal. B-Environ.* **2008**, *81*, 64–77. [[CrossRef](#)]
12. Rezaei, H.; Shafaei, S.Z.; Abdollahi, H.; Shahidi, A.; Ghassa, S. A sustainable method for germanium, vanadium and lithium extraction from coal fly ash: Sodium salts roasting and organic acids leaching. *Fuel* **2022**, *312*, 122844. [[CrossRef](#)]
13. Kaußen, F.M.; Friedrich, B. Methods for Alkaline Recovery of Aluminum from Bauxite Residue. *J. Sustain. Metall.* **2016**, *2*, 353–364. [[CrossRef](#)]
14. Bruckard, W.J.; Calle, C.M.; Davidson, R.H.; Glenn, A.M.; Jahanshahi, S. Smelting of bauxite residue to form a soluble sodium aluminium silicate phase to recover alumina and soda. *Miner. Process. Extr. Metall.* **2010**, *119*, 18–260. [[CrossRef](#)]
15. Li, X.B.; Xiao, W.; Liu, W.; Liu, G.H.; Peng, Z.H.; Zhou, Q.S.; Qi, T.G. Recovery of alumina and ferric oxide from Bayer red mud rich in iron by reduction sintering. *Trans. Nonferrous Met. Soc. China* **2009**, *19*, 1342–1347. [[CrossRef](#)]

16. Liu, W.; Sun, S.; Zhang, L.; Jahanshahi, S.; Yang, J. Experimental and simulative study on phase transformation in Bayer red mud soda-lime roasting system and recovery of Al, Na and Fe. *Miner. Eng.* **2012**, *39*, 213–218. [[CrossRef](#)]
17. Pei, J.; Pan, X.; Zhang, Y.; Yu, H.; Tu, G. A novel process to fully utilize red mud based on low-calcium sintering. *J. Environ. Chem. Eng.* **2021**, *9*, 106754. [[CrossRef](#)]
18. Rayapudi, V. Extraction of Iron values from Red mud. *Mater. Today Proc.* **2018**, *5*, 17064–17072.
19. Qi, Z.; Joshi, I.P.; Liu, R.; Li, Y.; Liu, H.; Qu, J. Adsorption combined with superconducting high gradient magnetic separation technique used for removal of arsenic and antimony. *J. Hazard. Mater.* **2018**, *343*, 36–48. [[CrossRef](#)]
20. Archambo, M.; Kawatra, S.K. Red Mud: Fundamentals and New Avenues for Utilization. *Miner. Process. Extr. Metall. Rev.* **2021**, *42*, 427–450. [[CrossRef](#)]
21. Rao, M.; Zhuang, J.; Li, G.; Zeng, J.; Jiang, T. Iron Recovery from Red Mud by Reduction Roasting-Magnetic Separation. In *Light Metals 2013*; Springer: Berlin/Heidelberg, Germany, 2013.
22. Ding, W.; Xiao, J.-H.; Peng, Y.; Shen, S.-Y.; Chen, T. Iron Extraction from Red Mud using Roasting with Sodium Salt. *Miner. Process. Extr. Metall. Rev.* **2021**, *42*, 153–161.
23. Li, G.; Liu, M.; Rao, M.; Jiang, T.; Zhuang, J.; Zhang, Y. Stepwise extraction of valuable components from red mud based on reductive roasting with sodium salts. *J. Hazard. Mater.* **2014**, *280*, 774–780. [[CrossRef](#)]
24. Ding, W.; Xiao, J.; Peng, Y.; Shen, S.; Chen, T.; Zou, K.; Wang, Z. A novel process for extraction of iron from a refractory red mud. *Physicochem. Probl. Miner. Process.* **2020**, *56*, 125–136. [[CrossRef](#)]
25. Gateshki, M.; Petkov, V.; Pradhan, S.K.; Vogt, T. Structure of nanocrystalline MgFe₂O₄ from X-ray diffraction, Rietveld and atomic pair distribution function analysis. *J. Appl. Crystallogr.* **2005**, *38*, 772–779. [[CrossRef](#)]
26. Foroughi, F.; Hassanzadeh-Tabrizi, S.A.; Bigham, A. In situ microemulsion synthesis of hydroxyapatite-MgFe₂O₄ nanocomposite as a magnetic drug delivery system. *Mater. Sci. Eng. C-Mater. Biol. Appl.* **2016**, *68*, 774–779. [[CrossRef](#)]
27. Manikandan, M.; Manimuthu, P.; Venkateswaran, C. Structural and Magnetic properties of MgFe₂O₄ Ceramic. In Proceedings of the 2nd International Conference on Optoelectronic Materials and Thin Films for Advanced Technology (OMTAT), Kochi, India, 3–5 January 2013; pp. 194–196.
28. Sattar, A.A.; Wafik, A.H.; Kandil, K.M. The effect of sintering temperature on microhardness and Barkhausen jumps of Ni and Mg ferrites. *J. Phys. D* **1996**, *29*, 25–28. [[CrossRef](#)]
29. Xue, P.; He, D.; Xu, A.; Gu, Z.; Yang, Q.; Engstrom, F.; Bjorkman, B. Modification of industrial BOF slag: Formation of MgFe₂O₄ and recycling of iron. *J. Alloy. Compd.* **2017**, *712*, 640–648. [[CrossRef](#)]
30. He, Z.; Lan, M.; Hu, X.; Xue, X.; Chou, K.-C. Study on Oxidation Behavior of Industrial Basic Oxygen Furnace Slag and Recovery of Magnetic Iron-Containing Phase. *Steel Res. Int.* **2022**, *93*, 2100558. [[CrossRef](#)]
31. He, L.; Shi, L.; Huang, Q.; Hayat, W.; Shang, Z.; Ma, T.; Wang, M.; Yao, W.; Huang, H.; Chen, R. Extraction of alumina from aluminum dross by a non-hazardous alkaline sintering process: Dissolution kinetics of alumina and silica from calcined materials. *Sci. Total Environ.* **2021**, *777*, 146123. [[CrossRef](#)]
32. Hodge, H.; Rowles, M.R.; Hayes, P.C.; Hawker, W.; Vaughan, J. Bauxite residue sinter leach process—Phases formation, reaction pathways and kinetics. *Miner. Process. Extr. Metall.* **2021**, *130*, 341–353. [[CrossRef](#)]
33. Qi, T.; Liu, N.; Li, X.; Peng, Z.; Liu, G.; Zhou, Q. Thermodynamics of chromite ore oxidative roasting process. *J. Cent. South Univ. Technol.* **2011**, *18*, 83–88. [[CrossRef](#)]
34. Thibodeau, E.; Gheribi, A.E.; Jung, I.-H. A Structural Molar Volume Model for Oxide Melts Part III: Fe Oxide-Containing Melts. *Metall. Mater. Trans. B* **2016**, *47*, 1187–1202. [[CrossRef](#)]
35. Eremin, N.I. Phase composition of aluminocalcium sinters in the system CaO-Al₂O₃-SiO₂-Na₂O-MgO-Fe₂O₃. *Inorg. Mater.* **1973**, *9*, 1102–1104.
36. Blackman, L. On the Formation of Fe²⁺ in the System MgO-Fe₂O₃-MgFe₂O₄ at High Temperatures. *J. Am. Ceram. Soc.* **1959**, *42*, 143–145. [[CrossRef](#)]
37. O'Neill, H.S.C.; Annersten, H.; Virgo, D. The temperature dependence of the cation distribution in magnesioferrite (MgFe₂O₄) from powder XRD structural refinements and Mössbauer spectroscopy. *Am. Mineral.* **1992**, *77*, 725–740.
38. Dieckmann, R.; Schmalzried, H. Defects and Cation Diffusion in Magnetite (I). In *Berichte Der Bunsengesellschaft Für Physikalische Chemie*; Wiley: Hoboken, NJ, USA, 1977.
39. Dieckmann, R.; Schmalzried, H. Defects and Cation Diffusion in Magnetite (II). In *Berichte Der Bunsengesellschaft Für Physikalische Chemie*; Wiley: Hoboken, NJ, USA, 1977.
40. Yang, J.; Sun, H.; Peng, T.; Zeng, L.; Chao, L. Separation of alumina from aluminum-rich coal fly ash using NaOH molten salt calcination and hydrochemical process. *Clean Technol. Environ. Policy* **2022**, *24*, 1507–1519. [[CrossRef](#)]
41. Whittington, B.I. The Chemistry of CaO and Ca(OH)₂ Relating to the Bayer Process. *Hydrometallurgy* **1996**, *43*, 13–35. [[CrossRef](#)]
42. Liu, G.H.; He, Q.; Li, X.B.; Peng, Z.H.; Zhou, Q.S. Synthesis and reaction behavior of calcium silicate hydrate in basic system. *Trans. Nonferrous Met. Soc. China* **2004**, *14*, 1204–1209.

Disclaimer/Publisher's Note: The statements, opinions and data contained in all publications are solely those of the individual author(s) and contributor(s) and not of MDPI and/or the editor(s). MDPI and/or the editor(s) disclaim responsibility for any injury to people or property resulting from any ideas, methods, instructions or products referred to in the content.